

Spin Dynamics in Hierarchical Black Hole Triples: Predicting Final Spin-Orbit Misalignment Angle From Initial Conditions

YUBO SU,¹ DONG LAI,¹ AND BIN LIU¹

¹*Cornell Center for Astrophysics and Planetary Science, Department of Astronomy, Cornell University, Ithaca, NY 14853, USA*

(Received XXXX; Revised XXXX; Accepted XXXX)

Submitted to ApJ

ABSTRACT

Abstract

Keywords: keywords

1. INTRODUCTION

As the LIGO/VIRGO collaboration continues to detect mergers of black hole (BH) binaries (e.g. Abbott et al. 2016, 2019), it is increasingly important to systematically study various formation channels of BH binaries and their observable signatures. The canonical channel consists of isolated binary evolution, in which mass transfer and friction in the common envelope phase cause the binary orbit to shrink sufficiently that it subsequently merges via emission of gravitational waves (GW) within a Hubble time (e.g. Lipunov et al. 1997, 2017; Podsiadlowski et al. 2003; Belczynski et al. 2010, 2016; Dominik et al. 2012, 2013, 2015). BH binaries formed via isolated binary evolution are generally expected to have small misalignment between the BH spin axis and the orbital angular momentum axis (Postnov & Kuranov 2019; Belczynski et al. 2020). On the other hand, various flavors of dynamical formation channels of BH binaries have also been studied. These involve either strong gravitational scatterings in dense clusters (e.g. Zwart & McMillan 1999; O’leary et al. 2006; Miller & Lauburg 2009; Banerjee et al. 2010; Downing et al. 2010; Ziosi et al. 2014; Rodriguez et al. 2015; Samsing & Ramirez-Ruiz 2017; Samsing & D’Orazio 2018; Rodriguez et al. 2018; Gondán et al. 2018) or more gentle “tertiary-induced mergers” (e.g. Blaes et al. 2002; Miller & Hamilton 2002; Wen 2003; Antonini & Perets 2012; Antonini et al. 2017; Silsbee & Tremaine 2016; Liu & Lai 2017, 2018; Randall & Xianyu 2018; Hoang et al. 2018). The dynamical formation channels generally produce BH binaries with misaligned spins.

GW observations of binary inspirals can put constraints on BH masses and spins. Typically, spin constraints come in the form of two dimensionless mass-weighted combinations of the component BH spins: (i) the aligned spin parameter

$$\chi_{\text{eff}} \equiv \frac{m_1 \chi_1 \cos \theta_{s_1,1} + m_2 \chi_2 \cos \theta_{s_2,1}}{m_1 + m_2} \quad (1)$$

where $m_{1,2}$ are the masses of the BHs, $\theta_{s_i,1}$ is the angle between the i th spin and the binary orbital angular momentum axis, and $\chi_i \equiv cS_i/(Gm_i^2)$ is the dimensionless Kerr spin parameter; and (ii) the perpendicular spin parameter (Schmidt et al. 2015)

$$\chi_p \equiv \max \left\{ \chi_1 \sin \theta_{s_1,1}, \frac{q(4q+3)}{4+3q} \chi_2 \sin \theta_{s_2,1} \right\}, \quad (2)$$

where $q \equiv m_2/m_1$. The systems detected in the O1 and O2 observing runs have small χ_{eff} , which is consistent with either small χ_1 and χ_2 or highly misaligned BH spins ($\theta_{s_i,1} \approx 90^\circ$).

TODO Update this paragraph later with references. In the recent GW detection GW190521.1, the component BHs have dimensionless spins $\chi_{1,2} = S_{1,2}/M_{1,2}^2 \sim 0.7$, yet $\chi_{\text{eff}} \approx 0$ while $\chi_p \sim 1$. This requires both BH spins be misaligned with the orbital angular momentum, i.e. $\theta_{s_i,1} \approx 90^\circ$.

Liu & Lai (2017, 2018, hereafter LL17, LL18), and Liu et al. (2019) carried out a systematic study of binary BH mergers in the presence of a tertiary companion. LL17 pointed out the important effect of spin-orbit coupling (de-Sitter precession) in determining the final spin-orbit misalignment angles of BH binaries in triple systems. They considered binaries with sufficiently compact orbits (so that mergers are possible even without a tertiary) and showed that the combination of LK oscillations (induced by a modestly inclined tertiary) and spin-orbit coupling gives rise to a broad range of final spin-orbit misalignment in the merging binary BHs. We call these mergers *LK-enhanced mergers*. LL18 considered the

most interesting case of *LK-induced mergers*, in which an initially wide BH binary (too wide to merge in isolation) is pushed to extreme eccentricities (close to unity) by a highly inclined tertiary and merges within a few Gyrs. LL18 examined a wide range of orbital and spin evolution behaviors and found that LK-induced mergers can sometimes yield a “90° attractor”: when the BH spin is initially aligned with the inner binary angular momentum axis ($\theta_{\text{sl}}^i = 0$), it evolves towards a perpendicular state ($\theta_{\text{sl}}^f = 90^\circ$) near merger. Qualitatively, they found that the attractor exists when the LK-induced orbital decay is sufficiently “gentle” and the octupole effect is unimportant. Fig. 1 gives an example of a system evolving towards this attractor, where θ_{sl} converges to $\approx 90^\circ$ at late times in the bottom right panel. Fig. 2 shows how θ_{sl}^f varies when the initial inclination of the tertiary orbit I_0 (relative to the inner orbit) is varied. Note that for rapid mergers (when I_0 is close to 90°), the attractor does not exist; as I_0 deviates more from 90° , the merger time increases and θ_{sl}^f is close to 90° . This 90° attractor gives rise to a peak around $\chi_{\text{eff}} = 0$ in the final χ_{eff} distribution in tertiary-induced mergers (LL18; Liu et al. 2019). This peak was also found in the population studies of Antonini et al. (2018).

The physical origin of this 90° attractor and under what conditions it can be achieved are not well understood. LL18 proposed an explanation based on analogy with an adiabatic invariant in systems where the inner binary remains circular throughout the inspiral (LL17). However, this analogy is not justified, as significant eccentricity excitation is a necessary ingredient in LK-induced mergers. In addition, the LK-enhanced mergers considered in LL17 show no 90° attractor even though the orbital evolution is slow and regular.

In this paper, we study an analytic theory that reproduces the 90° attractor and characterizes its regime of validity. In Sections 2 and 3, we set up the relevant equations of motion for the orbital and spin evolution of the system. In Sections 4 and 5, we develop an analytic theory and compute its regime of validity for LK-induced mergers. In Section 6, we comment on the LK-enhanced scenario. We discuss and conclude in Section 7.

2. LK-INDUCED MERGERS: ORBITAL EVOLUTION

In this section we summarize the key features and relevant equations for LK-induced mergers to be used for our analysis in later sections. Consider a black hole (BH) binary with masses m_1 and m_2 having total mass m_{12} , reduced mass $\mu = m_1 m_2 / m_{12}$, semimajor axis a and eccentricity e . This inner binary orbits around a tertiary with mass m_3 , semimajor axis a_{out} and eccentricity e_{out} in a hierarchical configuration ($a_{\text{out}} \gg a$). Unless explicitly stated, we assume $m_3 \gg m_1, m_2$ (so the tertiary is a supermassive black hole, or SMBH), although our analysis can be easily generalized to comparable masses. It is also convenient to define the effective outer

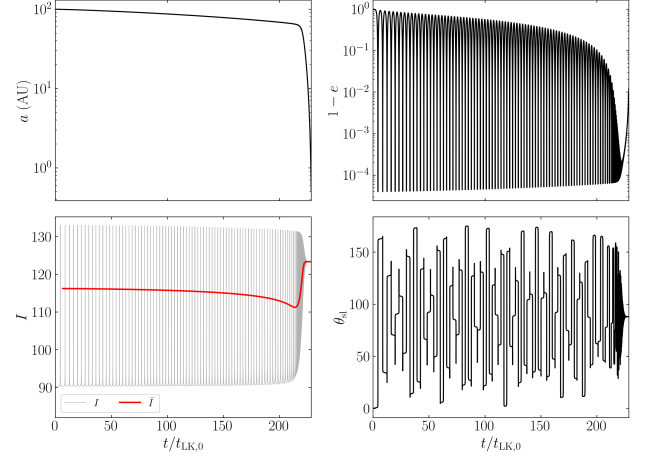


Figure 1. An example of the 90° spin attractor in LK-induced BH binary mergers. The four panels show the time evolution of the binary semi-major axis a , eccentricity e , inclination I [the red line denotes the averaged \bar{I} given by Eq. (29)], and spin-orbit misalignment angle θ_{sl} . The unit of time $t_{\text{LK},0}$ is the LK timescale [Eq. (10)] evaluated for the initial conditions. The inner binary has $m_1 = 30M_\odot$, $m_2 = 20M_\odot$, and initial $a_0 = 100$ AU, $e_0 = 0.001$, $I_0 = 90.35^\circ$ (with respect to the outer binary), and $\theta_{\text{sl}}^i = 0$. The tertiary SMBH has $a_{\text{out}} = 2.2$ pc, $e_{\text{out}} = 0$, and $m_3 = 3 \times 10^7 M_\odot$. It can be seen that θ_{sl} evolves to $\sim 90^\circ$ as a shrinks to smaller values.

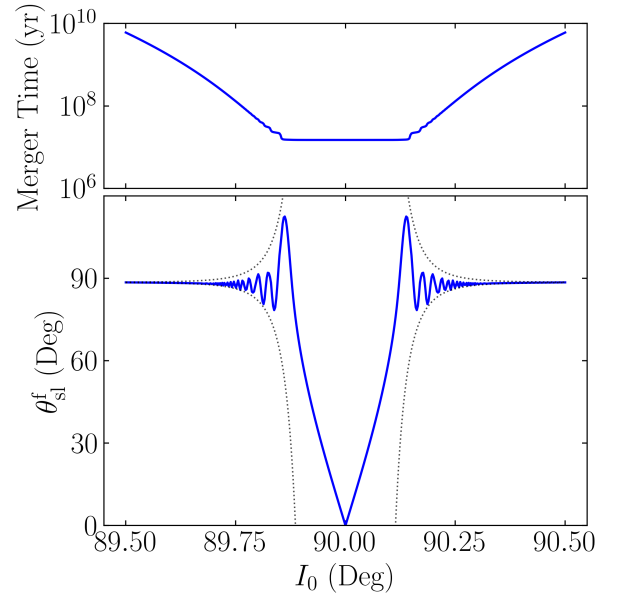


Figure 2. The merger time and the final spin-orbit misalignment angle θ_{sl}^f as a function of the initial inclination I_0 for LK-induced mergers. The other parameters are the same as those in Fig. 1. For I_0 somewhat far away from 90° , the resulting θ_{sl}^f are all quite near 90° . The black dashed line in the lower panel shows Eq. (59), which provides an estimate for the deviation from the 90° attractor.

semimajor axis

$$\tilde{a}_{\text{out}} \equiv a_{\text{out}} \sqrt{1 - e_{\text{out}}^2}. \quad (3)$$

We denote the orbital angular momentum of the inner binary by $\mathbf{L} \equiv L\hat{\mathbf{L}}$ and the angular momentum of the outer binary by $\mathbf{L}_{\text{out}} \equiv L_{\text{out}}\hat{\mathbf{L}}_{\text{out}}$. Since $L_{\text{out}} \gg L$, we take \mathbf{L}_{out} to be fixed.

The equations of motion governing the orbital elements a , e , φ , I , ω (where φ , I , ω are the longitude of the ascending node, inclination, and argument of periapsis respectively) of the inner binary are

$$\frac{da}{dt} = \left(\frac{da}{dt} \right)_{\text{GW}}, \quad (4)$$

$$\frac{de}{dt} = \frac{15}{8t_{\text{LK}}} e j(e) \sin 2\omega \sin^2 I + \left(\frac{de}{dt} \right)_{\text{GW}}, \quad (5)$$

$$\frac{d\varphi}{dt} = \frac{3}{4t_{\text{LK}}} \frac{\cos I (5e^2 \cos^2 \omega - 4e^2 - 1)}{j(e)}, \quad (6)$$

$$\frac{dI}{dt} = \frac{15}{16} \frac{e^2 \sin 2\omega \sin 2I}{j(e)}, \quad (7)$$

$$\frac{d\omega}{dt} = \frac{3}{4t_{\text{LK}}} \frac{2j^2(e) + 5 \sin^2 \omega (e^2 - \sin^2 I)}{j(e)} + \Omega_{\text{GR}}, \quad (8)$$

where we have defined

$$j(e) = \sqrt{1 - e^2}, \quad (9)$$

$$t_{\text{LK}}^{-1} \equiv n \left(\frac{m_3}{m_{12}} \right) \left(\frac{a}{\tilde{a}_{\text{out}}} \right)^3, \quad (10)$$

with $n \equiv \sqrt{Gm_{12}/a^3}$ the mean motion of the inner binary. The GR-induced apsidal precession of the inner binary is given by

$$\Omega_{\text{GR}}(e) = \frac{3Gnm_{12}}{c^2 a j^2(e)}. \quad (11)$$

The dissipative terms due to gravitational radiation are

$$\left(\frac{da}{dt} \right)_{\text{GW}} = -\frac{a}{t_{\text{GW}}(e)}, \quad (12)$$

$$\left(\frac{de}{dt} \right)_{\text{GW}} = -\frac{304}{15} \frac{G^3 \mu m_{12}^2}{c^5 a^4} \frac{1}{j^{5/2}(e)} \left(1 + \frac{121}{304} e^2 \right), \quad (13)$$

where

$$t_{\text{GW}}^{-1}(e) \equiv \frac{64}{5} \frac{G^3 \mu m_{12}^2}{c^5 a^4} \frac{1}{j^{7/2}(e)} \left(1 + \frac{73}{24} e^2 + \frac{37}{96} e^4 \right). \quad (14)$$

Fig. 1 depicts an example of LK-induced mergers as calculated using the above equations. We adopt the following fiducial parameters: the inner binary has $m_1 = 30M_{\odot}$, $m_2 = 20M_{\odot}$, initial $a = 100$ AU, $e_0 = 0.001$, and $I_0 = 90.35^\circ$. We take the SMBH tertiary companion to have $m_3 = 3 \times 10^7 M_{\odot}$ and $\tilde{a}_{\text{out}} = 4.5 \times 10^5$ AU = 2.2 pc. Since $\tilde{a}_{\text{out}} \gg a$, the octupole effects are negligible and have

been omitted in Eqs. (5–8). Note that these parameters give the same t_{LK} as Fig. 4 of LL18. We refer to this as the fiducial parameter regime, and our analysis in later sections will be based on this example unless otherwise noted.

We next discuss the key analytical properties of the orbital evolution.

2.1. Analytical Results Without GW Radiation

First, neglecting the GW radiation terms, the system admits two conservation laws, the “Kozai constant” and energy conservation,

$$j(e) \cos I = \text{const}, \quad (15)$$

$$\frac{3}{8} [2e^2 + j^2(e) \cos^2 I - 5e^2 \sin^2 I \sin^2 \omega] + \frac{\epsilon_{\text{GR}}}{j(e)} = \text{const}, \quad (16)$$

(see Anderson et al. (2016), LL18 for more general expressions when L_{out} is comparable to L), where

$$\epsilon_{\text{GR}} \equiv (\Omega_{\text{GR}} t_{\text{LK}})_{e=0} = \frac{3Gm_{12}^2 \tilde{a}_{\text{out}}^3}{c^2 m_3 a^4}. \quad (17)$$

The conservation laws can be combined to obtain the maximum eccentricity e_{max} as a function of the initial I_0 (and initial $e_0 \ll 1$). The largest value of e_{max} occurs at $I_0 = 90^\circ$ and is given by

$$j(e_{\text{max}})_{I_0=90^\circ} = (8/9)\epsilon_{\text{GR}}. \quad (18)$$

Eccentricity excitation then requires $\epsilon_{\text{GR}} < 9/8$. Our fiducial examples in Figs. 1 and 2 satisfy $\epsilon_{\text{GR}} \ll 1$ at $a = a_0$, leading to $e_{\text{max}} \sim 1$ within a narrow inclination window around $I_0 = 90^\circ$.

Eqs. (15) and (16) imply that e is a function of $\sin^2 \omega$ alone (see Kinoshita 1993; Storch & Lai 2015, for exact forms), so an eccentricity maximum occurs every half period of ω . We define the period and angular frequency of eccentricity oscillation via

$$\pi = \int_0^{P_{\text{LK}}} \frac{d\omega}{dt} dt, \quad \Omega_{\text{LK}} \equiv \frac{2\pi}{P_{\text{LK}}}. \quad (19)$$

In LK cycles, the inner binary oscillates between the eccentricity minimum e_{min} and maximum e_{max} . The oscillation is “uneven”: when $e_{\text{min}} \ll e_{\text{max}}$, the binary spends a fraction $\sim j(e_{\text{max}})$ of the LK cycle, or time $\Delta t \sim t_{\text{LK}} j(e_{\text{max}})$, near $e \simeq e_{\text{max}}$ (see Eq. (8)).

2.2. Behavior with GW Radiation

Including the effect of GW radiation, orbital decay predominantly occurs at $e \simeq e_{\text{max}}$ with the timescale of $t_{\text{GW}}(e_{\text{max}})$ [see Eq. (14)]. On the other hand, Eq. (8) implies that, when $\epsilon_{\text{GR}} \ll 1$, the binary spends only a small fraction ($\sim j(e_{\text{max}})$) of the time near $e \simeq e_{\text{max}}$. Thus, we expect two qualitatively different merger behaviors:

- “Rapid mergers”: When $t_{\text{GW}}(e_{\text{max}}) \lesssim t_{\text{LK}}j(e_{\text{max}})$, the binary is “pushed” into high eccentricity and exhibits a “one shot merger” without any e -oscillations.
- “Smooth mergers”: When $t_{\text{GW}}(e_{\text{max}}) \gtrsim t_{\text{LK}}j(e_{\text{max}})$, the binary goes through a phase of eccentricity oscillations while the orbit gradually decays. In this case, the LK-averaged orbital decay rate is $\sim j(e_{\text{max}})t_{\text{GW}}^{-1}(e_{\text{max}})$. As a decreases, e_{max} decreases slightly while the minimum eccentricity increases, approaching e_{max} (see Fig. 1). This eccentricity oscillation “freeze” ($e_{\text{min}} \sim e_{\text{max}}$) is due to GR-induced apsidal precession (ϵ_{GR} increases as a decreases), and occurs when $\epsilon_{\text{GR}}(a) \gg j(e_{\text{max}})$. After the eccentricity is frozen, the binary circularizes and decays on the timescale $t_{\text{GW}}(e_{\text{max}})$.

3. SPIN DYNAMICS: EQUATIONS

We are interested in the spin orientations of the inner BHs at merger as a function of initial conditions. Since they evolve independently to leading post-Newtonian order, we focus on the dynamics of $\hat{\mathbf{S}}_1 = \hat{\mathbf{S}}$, the spin vector of m_1 . Since the spin magnitude does not enter into the dynamics, we write $\mathbf{S} \equiv \hat{\mathbf{S}}$ for brevity (i.e. \mathbf{S} is a unit vector). Neglecting spin-spin interactions, \mathbf{S} undergoes de Sitter precession about \mathbf{L} as

$$\frac{d\mathbf{S}}{dt} = \Omega_{\text{SL}} \hat{\mathbf{L}} \times \mathbf{S}, \quad (20)$$

with

$$\Omega_{\text{SL}} = \frac{3Gn(m_2 + \mu/3)}{2c^2 a j^2(e)}. \quad (21)$$

In the presence of a tertiary companion, the orbital axis $\hat{\mathbf{L}}$ of the inner binary precesses around $\hat{\mathbf{L}}_{\text{out}}$ with rate $d\varphi/dt$ and nutates with varying I [see Eqs. (6) and (7)]. To analyze the dynamics of the spin vector, we go to the co-rotating frame with $\hat{\mathbf{L}}$ about $\hat{\mathbf{L}}_{\text{out}}$, in which Eq. (20) becomes

$$\left(\frac{d\mathbf{S}}{dt} \right)_{\text{rot}} = \mathbf{\Omega}_e \times \mathbf{S}, \quad (22)$$

where we have defined an effective rotation vector

$$\mathbf{\Omega}_e \equiv \Omega_{\text{L}} \hat{\mathbf{L}}_{\text{out}} + \Omega_{\text{SL}} \hat{\mathbf{L}}, \quad (23)$$

with [see Eq. (6)]

$$\Omega_{\text{L}} \equiv -\frac{d\varphi}{dt}. \quad (24)$$

In this rotating frame, the plane spanned by $\hat{\mathbf{L}}_{\text{out}}$ and $\hat{\mathbf{L}}$ is constant in time, only the inclination angle I can vary.

3.1. Nondissipative Dynamics

We first consider the limit where dissipation via GW radiation is completely neglected ($t_{\text{GW}}(e) \rightarrow \infty$). Then $\mathbf{\Omega}_e$ is exactly periodic with period P_{LK} [see Eq. (19)] We can rewrite Eq. (22) in Fourier components

$$\left(\frac{d\mathbf{S}}{dt} \right)_{\text{rot}} = \left[\bar{\mathbf{\Omega}}_e + \sum_{N=1}^{\infty} \mathbf{\Omega}_{eN} \cos(N\Omega_{\text{LK}}t) \right] \times \mathbf{S}. \quad (25)$$

We write $\bar{\mathbf{\Omega}}_e \equiv \mathbf{\Omega}_{e0}$ for convenience, where the bar denotes an average over a LK cycle. We have adopted the convention where $t = 0$ is the time of maximum eccentricity of the LK cycle, so that Eq. (25) does not have $\sin(N\Omega_{\text{LK}}t)$ terms.

This system superficially resembles that considered in Storch & Lai (2015) (SL15), who studied the dynamics of the spin axis of a star when driven by a giant planet undergoing LK oscillations (see also Storch et al. 2014, 2017). In their system, the spin-orbit coupling arises from Newtonian interaction between the planet (M_{p}) and the rotation-induced stellar quadrupole ($I_{\text{out}} - I_1$), and the spin precession frequency is

$$\Omega_{\text{SL}}^{(\text{Newtonian})} = -\frac{3GM_{\text{p}}(I_{\text{out}} - I_1) \cos \theta_{\text{sl}}}{2a^3 j^3(e) I_3 \Omega_{\text{s}}}, \quad (26)$$

where $I_3 \Omega_{\text{s}}$ is the spin angular momentum of the star. SL15 showed that under some conditions that depend on a dimensionless adiabaticity parameter (roughly the ratio between the magnitudes of $\Omega_{\text{SL}}^{(\text{Newtonian})}$ and Ω_{L} when factoring out the eccentricity and obliquity dependence), the stellar spin axis can vary chaotically. One strong indicator of chaos in their study is the presence of irregular, fine structure in a bifurcation diagram [Fig. 1 of Storch & Lai (2015)] that shows the values of the spin-orbit misalignment angle θ_{sl} when varying system parameters in the “transadiabatic” regime, where the adiabaticity parameter crosses unity.

To generate an analogous bifurcation diagram for our problem, we consider a sample system with $m_{12} = 60M_{\odot}$, $m_3 = 3 \times 10^7 M_{\odot}$, $a = 0.1 \text{ AU}$, $e_0 = 10^{-3}$, $I_0 = 70^\circ$, $a_{\text{out}} = 300 \text{ AU}$, $e_{\text{out}} = 0$, and initial $\theta_{\text{sl}} = 0$. We then evolve Eq. (22) together with the orbital evolution equations [Eqs. (4–8) without the GW terms] while sampling both θ_{sl} and θ_e at eccentricity maxima, where θ_e is given by

$$\cos \theta_e = \frac{\bar{\mathbf{\Omega}}_e}{\Omega_e} \cdot \mathbf{S}. \quad (27)$$

We repeat this procedure with different mass ratios m_1/m_{12} of the inner binary, which only changes Ω_{SL} without changing the orbital evolution (note that the LK oscillation depends only on m_{12} and not on individual masses of the inner binary). Analogous to SL15, we consider systems with a range of the adiabaticity parameter \mathcal{A} [to be defined later in Eq. (31)] that

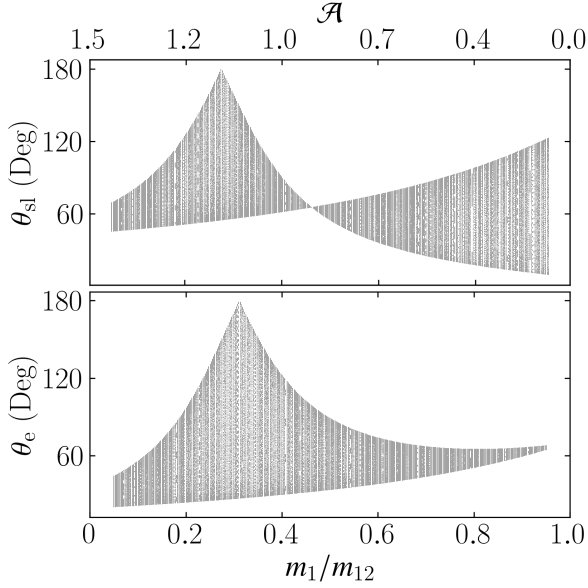


Figure 3. Bifurcation diagram for the BH spin orientation during LK oscillations. The physical parameters are $m_{12} = 60M_{\odot}$, $m_3 = 3 \times 10^7 M_{\odot}$, $a = 0.1$ AU, $e_0 = 10^{-3}$, $I_0 = 70^\circ$, $a_{\text{out}} = 300$ AU, $e_{\text{out}} = 0$, and initial condition $\theta_{\text{sl}}^i = 0$. For each mass ratio m_1/m_{12} , the orbit-spin system is solved over 500 LK cycles, and both θ_{sl} (the angle between \mathbf{S} and $\hat{\mathbf{L}}$) and θ_e [defined by Eq. (27)] are sampled at every eccentricity maximum and are plotted. The top axis shows the adiabaticity parameter \mathcal{A} as defined by Eq. (31). Note that for a given m_{12} , changing the mass ratio m_1/m_{12} only changes the spin evolution and not the orbital evolution.

crosses order unity. The fiducial system of Fig. 1 does not serve this purpose because the initial Ω_{SL} is too small. Our result is depicted in Fig. 3.

While our bifurcation diagram has interesting structure, the features are all regular. This is in contrast to the star-planet system studied by SL15 (see their Fig. 1). A key difference is that in our system, Ω_{SL} does not depend on θ_{sl} , while for the planet-star system, $\Omega_{\text{SL}}^{(\text{Newtonian})}$ does, and this latter feature introduces nonlinearity to the dynamics.

A more formal understanding of the dynamical behavior of our spin-orbit system comes from Floquet theory (Floquet 1883; Kuchment 2012), as Eq. (22) is a linear system with periodic coefficients (the system studied in SL15 is nonlinear). Floquet’s theorem says that when a linear system with periodic coefficients is integrated over a period, the evolution can be described by the linear transformation

$$\mathbf{S}(t + P_{\text{LK}}) = \tilde{\mathbf{M}}\mathbf{S}(t), \quad (28)$$

where $\tilde{\mathbf{M}}$ is called the *monodromy matrix* and is independent of \mathbf{S} .

For our system, while $\tilde{\mathbf{M}}$ can be easily defined, it cannot be evaluated in closed form. Thankfully, it suffices to reason directly about the general properties of $\tilde{\mathbf{M}}$: it must be a proper

orthogonal matrix, or a rotation matrix, as it represents the effect of many infinitesimal rotations, each about the instantaneous Ω_e ¹. Therefore, over each period P_{LK} , the dynamics of \mathbf{S} are equivalent to a rotation about a fixed axis, prohibiting chaotic behavior.

Another traditional indicator of chaos is a positive Lyapunov exponent, obtained when the separation between nearby trajectories diverges *exponentially* in time. In Floquet theory, the Lyapunov exponent is the logarithm of the largest eigenvalue of the monodromy matrix. Since $\tilde{\mathbf{M}}$ is a rotation matrix in our problem, the Lyapunov exponent must be 0, indicating no chaos. We have verified this numerically.

3.2. Spin Dynamics With GW Dissipation

When t_{GW} is finite, the coefficients Ω_{eN} , including $\bar{\Omega}_e = \Omega_{e0}$ [see Eq. (25)], are no longer constant, but change over time. For “smooth” mergers (satisfying $t_{\text{GW}}(e_{\text{max}}) \gg t_{\text{LK}}j(e_{\text{max}})$; see Section 2), the binary goes through a sequence of LK cycles, and the coefficients vary on the LK-averaged orbital decay time $t_{\text{GW}}(e_{\text{max}})/j(e_{\text{max}})$. As the LK oscillation freezes, we have $\Omega_e \approx \bar{\Omega}_e$ (and $\Omega_{eN} \approx 0$ for $N \geq 1$), which evolves on timescale $t_{\text{GW}}(e)$ as the orbit decays and circularizes.

Once a is sufficiently small such that $\Omega_{\text{SL}} \gg \Omega_L$ (this also corresponds to $\epsilon_{\text{GR}} \gg 1$ since $\Omega_{\text{SL}} \sim \Omega_{\text{GR}}$, implying the LK cycles are suppressed), it can be seen from Eqs. (22–23) that $\theta_e = \theta_{\text{sl}}$ is constant, i.e. the spin-orbit misalignment angle is frozen (see bottom right panel of Fig. 1). This is the “final” spin-orbit misalignment, although the binary may still be far from the final merger. For the fiducial examples depicted in Figs. 1–2, we stop the simulation at $a = 0.5$ AU, as θ_{sl} has converged to its final value.

3.3. Spin Dynamics Equation in Component Form

For later analysis, it is useful to write Eq. (25) in component form. To do so, we define inclination angle \bar{I}_e as the angle between $\bar{\Omega}_e$ and \mathbf{L}_{out} as shown in Fig. 4. To express \bar{I}_e algebraically, we define LK-averaged quantities

$$\overline{\Omega_{\text{SL}} \sin \bar{I}} \equiv \bar{\Omega}_{\text{SL}} \sin \bar{I}, \quad \overline{\Omega_{\text{SL}} \cos \bar{I}} \equiv \bar{\Omega}_{\text{SL}} \cos \bar{I}. \quad (29)$$

It then follows from Eq. (23) that

$$\tan \bar{I}_e = \frac{\mathcal{A} \sin \bar{I}}{1 + \mathcal{A} \cos \bar{I}}, \quad (30)$$

where \mathcal{A} is the adiabaticity parameter, given by

$$\mathcal{A} \equiv \frac{\bar{\Omega}_{\text{SL}}}{\Omega_L}. \quad (31)$$

¹ More formally, $\tilde{\mathbf{M}} = \tilde{\Phi}(P_{\text{LK}})$ where $\tilde{\Phi}(t)$ is the *principal fundamental matrix solution*: the columns of $\tilde{\Phi}$ are solutions to Eq. (22) and $\tilde{\Phi}(0)$ is the identity. By linearity, the columns of $\tilde{\Phi}(t)$ remain orthonormal, while its determinant does not change, so $\tilde{\mathbf{M}}$ is a proper orthogonal matrix, or a rotation matrix.

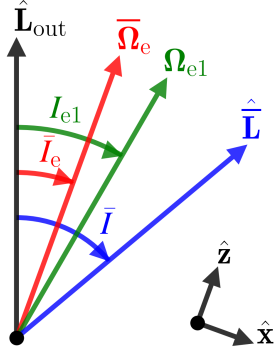


Figure 4. Definition of angles in the problem, shown in plane of the two angular momenta \mathbf{L}_{out} and \mathbf{L} . Here, $\bar{\mathbf{L}}$ is the suitably averaged \mathbf{L} with inclination \bar{I} defined by Eq. (29), $\bar{\Omega}_e$ is the LK-averaged Ω_e , and Ω_{e1} is the first harmonic component (see Eqs. (23) and (25)). Note that for $I_0 > 90^\circ$ (and $\bar{I} > 90^\circ$), we have $\bar{I}_e \in (90^\circ, 180^\circ)$ since $\Omega_L < 0$. The bottom right shows our choice of coordinate axes with $\hat{\mathbf{z}} \propto \bar{\Omega}_e$.

Note that in Eq. (30), \bar{I}_e is defined in the domain $[0^\circ, 180^\circ]$, i.e. $\bar{I}_e \in (0, 90)$ when $\tan \bar{I}_e > 0$ and $\bar{I}_e \in (90, 180)$ when $\tan \bar{I}_e < 0$.

We now choose a non-inertial coordinate system where $\hat{\mathbf{z}} \propto \bar{\Omega}_e$ and $\hat{\mathbf{x}}$ lies in the plane of \mathbf{L}_{out} and \mathbf{L} (see Fig. 4). In this reference frame, the spin orientation is specified by the polar angle $\bar{\theta}_e$ as defined above in Eq. (36), and the equation of motion becomes

$$\left(\frac{d\mathbf{S}}{dt} \right)_{\text{xyz}} = \left[\bar{\Omega}_e \hat{\mathbf{z}} + \sum_{N=1}^{\infty} \Omega_{eN} \cos(N\Omega_{LK}t) \right] \times \mathbf{S} - \dot{\bar{I}}_e \hat{\mathbf{y}} \times \mathbf{S}. \quad (32)$$

One further simplification lets us cast this vector equation of motion into a scalar form. Break \mathbf{S} into components $\mathbf{S} = S_x \hat{\mathbf{x}} + S_y \hat{\mathbf{y}} + \cos \bar{\theta}_e \hat{\mathbf{z}}$ and define complex variable

$$S_{\perp} \equiv S_x + iS_y. \quad (33)$$

Then, we can rewrite Eq. (32) as

$$\frac{dS_{\perp}}{dt} = i\bar{\Omega}_e S_{\perp} - \dot{\bar{I}}_e \cos \bar{\theta}_e + \sum_{N=1}^{\infty} \left[\cos(\Delta I_{eN}) S_{\perp} - i \cos \bar{\theta}_e \sin(\Delta I_{eN}) \right] \Omega_{eN} \cos(N\Omega_{LK}t), \quad (34)$$

where Ω_{eN} is the magnitude of the vector Ω_{eN} (see Eq. (25)) and $\Delta I_{eN} = I_{eN} - \bar{I}_e$ where I_{eN} is the angle between Ω_{eN} and \mathbf{L}_{out} (see Fig. 4).

4. ANALYSIS: APPROXIMATE ADIABATIC INVARIANT

In general, Eqs. (25) and (34) are difficult to study analytically. In this section, we neglect the harmonic terms and focus on how the varying $\bar{\Omega}_e$ affects the evolution of the BH spin axis. The effect of the harmonic terms is studied in Section 5.

4.1. The Adiabatic Invariant

When neglecting the $N \geq 1$ harmonic terms, Eq. (25) reduces to

$$\left(\frac{d\bar{\mathbf{S}}}{dt} \right)_{\text{rot}} = \bar{\Omega}_e \times \bar{\mathbf{S}}. \quad (35)$$

It is not obvious to what extent the analysis of Eq. (35) is applicable to Eq. (25). From our numerical calculations, we find that the LK-average of \mathbf{S} often evolves following Eq. (35), motivating our notation $\bar{\mathbf{S}}$. Over timescales shorter than the LK period P_{LK} , Eq. (35) loses accuracy as the evolution of \mathbf{S} itself is dominated by the $N \geq 1$ harmonics we have neglected. An intuitive interpretation of this result is that the $N \geq 1$ harmonics vanish when integrating Eq. (25) over a LK cycle.

Eq. (35) has one desirable property: $\bar{\theta}_e$, given by

$$\cos \bar{\theta}_e \equiv \bar{\mathbf{S}} \cdot \frac{\bar{\Omega}_e}{\Omega_e}, \quad (36)$$

is an adiabatic invariant. The adiabaticity condition requires the precession axis evolve slowly compared to the precession frequency at all times, i.e.

$$\left| \frac{d\bar{I}_e}{dt} \right| \ll \bar{\Omega}_e. \quad (37)$$

For our fiducial example depicted in Fig. 1, the values of $\dot{\bar{I}}_e$ and $\bar{\Omega}_e$ are shown in the top panel of Fig. 5, and the evolution of $\bar{\theta}_e$ in the bottom panel. The net change in $\bar{\theta}_e$ in this simulation is 0.01° , small as expected since $\left| \dot{\bar{I}}_e \right| \ll \left| \bar{\Omega}_e \right|$ at all times.

4.2. Deviation from Adiabaticity

The extent to which $\bar{\theta}_e$ is conserved depends on how well Eq. (37) is satisfied. In this subsection, we derive a bound on the total non-conservation of $\bar{\theta}_e$, then in the next subsection we show how this bound can be estimated from initial conditions.

When neglecting harmonic terms, the scalar equation of motion Eq. (34) becomes

$$\frac{dS_{\perp}}{dt} = i\bar{\Omega}_e S_{\perp} - \dot{\bar{I}}_e \cos \bar{\theta}_e. \quad (38)$$

This can be solved in closed form. Defining

$$\Phi(t) \equiv \int^t \bar{\Omega}_e dt, \quad (39)$$

we obtain the solution between the initial time t_i and the final time t_f :

$$e^{-i\Phi} S_{\perp} \Big|_{t_i}^{t_f} = - \int_{t_i}^{t_f} e^{-i\Phi(\tau)} \dot{\bar{I}}_e \cos \bar{\theta}_e d\tau. \quad (40)$$

Recalling $|S_\perp| = \sin \bar{\theta}_e$ and analyzing Eq. (40), we see that $\bar{\theta}_e$ oscillates about its initial value with amplitude

$$|\Delta \bar{\theta}_e| \sim \left| \frac{\dot{\bar{I}}_e}{\bar{\Omega}_e} \right|. \quad (41)$$

In the adiabatic limit [Eq. (37)], $\bar{\theta}_e$ is indeed conserved, as the right-hand side of Eq. (41) goes to zero. The bottom panel of Fig. 5 shows $\Delta \bar{\theta}_e$ for the fiducial example. Note that $\bar{\theta}_e$ is indeed mostly constant where Eq. (41) predicts small oscillations.

If we denote $|\Delta \bar{\theta}_e|^f$ to be the net change in $\bar{\theta}_e$ over $t \in [t_i, t_f]$, we can give a loose bound

$$|\Delta \bar{\theta}_e|^f \lesssim \left| \frac{\dot{\bar{I}}_e}{\bar{\Omega}_e} \right|_{\max}. \quad (42)$$

Inspection of Fig. 5 indicates that the spin dynamics are mostly uninteresting except near the peak of $|\dot{\bar{I}}_e|$, which occurs where $\bar{\Omega}_{\text{SL}} \simeq |\Omega_L|$. We present a zoomed-in view of dynamical quantities near the peak of $\dot{\bar{I}}_e$ in Fig. 6. In particular, in the bottom-rightmost panel, we see that the fluctuations in $\bar{\theta}_e$ are dominated by a second contribution, the subject of the discussion in Section 5.

For comparison, we show in Fig. 7 a more rapid binary merger starting with $I_0 = 90.2^\circ$, for which $|\Delta \theta_e|^f \approx 2^\circ$. If we again examine the bottom-rightmost panel, we see that the net $|\Delta \bar{\theta}_e|^f$ obeys Eq. (42).

4.3. Estimate of Deviation from Adiabaticity from Initial Conditions

To estimate Eq. (42) as a function of initial conditions, we first differentiate Eq. (30),

$$\dot{\bar{I}}_e = \left(\frac{\dot{\mathcal{A}}}{\mathcal{A}} \right) \frac{\mathcal{A} \sin \bar{I}}{1 + 2\mathcal{A} \cos \bar{I} + \mathcal{A}^2}. \quad (43)$$

It also follows from Eq. (23) that

$$\bar{\Omega}_e = |\bar{\Omega}_L| \left(1 + 2\mathcal{A} \cos \bar{I} + \mathcal{A}^2 \right)^{1/2}, \quad (44)$$

from which we obtain

$$\left| \frac{\dot{\bar{I}}_e}{\bar{\Omega}_e} \right| = \left(\frac{\dot{\mathcal{A}}}{\mathcal{A}} \right) \frac{1}{|\bar{\Omega}_L|} \frac{\mathcal{A} \sin \bar{I}}{(1 + 2\mathcal{A} \cos \bar{I} + \mathcal{A}^2)^{3/2}}. \quad (45)$$

Moreover, if we assume the eccentricity is frozen around $e \simeq 1$ and use $\cos^2 \omega \simeq 1/2$ in $|\Omega_L| = |d\delta/dt|$, we obtain the estimate

$$\begin{aligned} \mathcal{A} &\simeq \frac{3Gn(m_2 + \mu/3)}{2c^2 a j^2(e)} \left[\frac{15 \cos \bar{I}}{8 t_{\text{LK}} j(e)} \right]^{-1} \\ &\simeq \frac{4}{5} \frac{G(m_2 + \mu/3) m_{12} \tilde{a}_{\text{out}}^3}{c^2 m_3 a^4 j(e) \cos \bar{I}}, \end{aligned} \quad (46)$$

$$\frac{\dot{\mathcal{A}}}{\mathcal{A}} = -4 \left(\frac{\dot{a}}{a} \right)_{\text{GW}} + \frac{e}{j^2(e)} \left(\frac{de}{dt} \right)_{\text{GW}}. \quad (47)$$

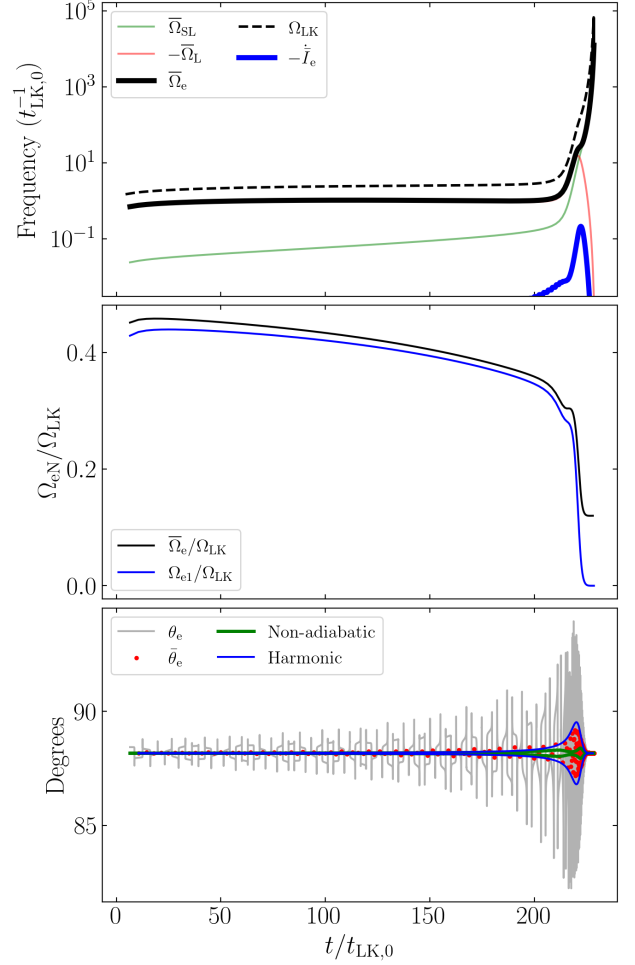


Figure 5. The same simulation as depicted in Fig. 1 but showing the calculated quantities relevant to the theory of the spin evolution. Top: the four characteristic frequencies of the system and $d\bar{I}_e/dt$. Middle: the frequency ratios between the zeroth and first Fourier components of Ω_e to the LK frequency Ω_{LK} . Bottom: Time evolution of θ_e [grey line; Eq. (27)], $\bar{\theta}_e$ [red dots; Eq. (36)], as well as estimates of the deviations from perfect conservation of $\bar{\theta}_e$ due to non-adiabaticity [green, Eq. (41)] and due to resonances with harmonic terms [blue, Eq. (63)].

With these, we see that Eq. (45) is largest around $\mathcal{A} \simeq 1$, and so we find that the maximum $|\dot{\bar{I}}_e/\bar{\Omega}_e|$ is given by

$$\left| \frac{\dot{\bar{I}}_e}{\bar{\Omega}_e} \right|_{\max} \simeq \left| \frac{\dot{\mathcal{A}}}{\mathcal{A}} \right| \frac{1}{|\bar{\Omega}_L|} \frac{\sin \bar{I}}{(2 + 2 \cos \bar{I})^{3/2}}. \quad (48)$$

To evaluate this, we make two assumptions: (i) \bar{I} is approximately j -e constant (see the third panels of Figs. 6 and 7), and (ii) $j(e)$ evaluated at $\mathcal{A} \simeq 1$ can be approximated as a constant multiple of the initial $j(e_{\text{max}})$, i.e.

$$j_\star \equiv j(e_\star) = f \sqrt{\frac{5}{3} \cos^2 I_0}, \quad (49)$$

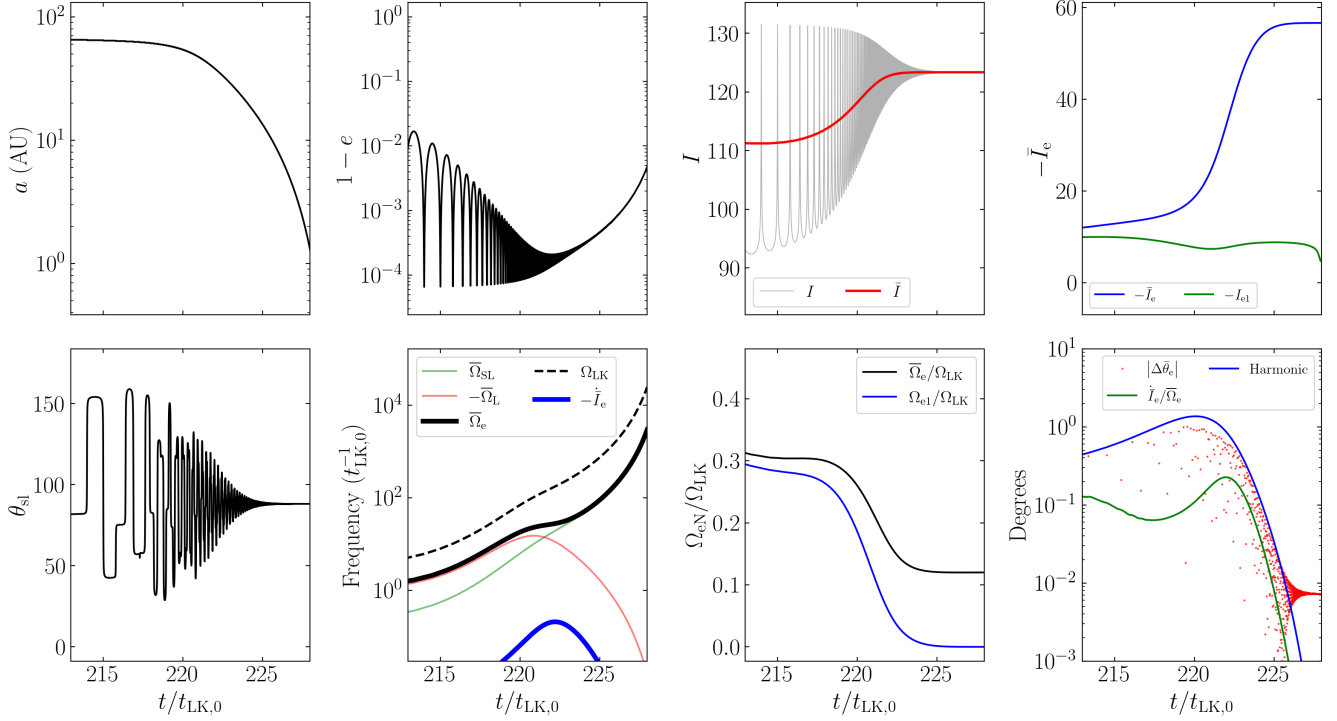


Figure 6. The same simulation as Fig. 1 but zoomed in on the region around $\mathcal{A} \equiv \bar{\Omega}_{\text{SL}}/\bar{\Omega}_L \simeq 1$ and showing a wide range of relevant quantities. The first three panels in the upper row depict a , e , I and \bar{I} as in Fig. 1, while the fourth shows \dot{I}_e [Eq. (30)] and \dot{I}_{e1} . The bottom four panels depict θ_{sl} , the four characteristic frequencies of the system and $d\dot{I}_e/dt$ [Eqs. 23 and (24)] (as in the top panel of Fig. 5), the relevant frequency ratios (as in the middle panel of Fig. 5), and the deviation of $\bar{\theta}_e$ from its initial value compared to the predictions of Eqs. (41) and (63).

where the star subscript denotes evaluation at $\mathcal{A} \simeq 1$ and $f > 1$ is a constant. Eq. (49) assumes that I_0 far enough from 90° that the GR effect is unimportant in determining e_{max} . The value of f turns out to be relatively insensitive to I_0 .

Using Eq. (47) and approximating $e_\star \approx 1$ in Eqs. (12) and (13) give

$$\left[\frac{\dot{\mathcal{A}}}{\mathcal{A}} \right]_\star \simeq \frac{G^3 \mu m_{12}^2}{c^5 a_\star^4 j_\star^7} \frac{595}{3}. \quad (50)$$

To determine a_\star , we require Eq. (46) to give $\mathcal{A} = 1$ for a_\star and j_\star . Taking this and Eq. (50), we rewrite Eq. (45) as

$$\left| \frac{\dot{I}_e}{\bar{\Omega}_e} \right|_{\text{max}} \simeq \frac{595 \sin \bar{I} |\cos \bar{I}|^{3/8}}{36 (\cos \bar{I} + 1)^{3/2}} \left[\frac{8000 G^9 m_{12}^9 m_3^3 \mu^8}{\bar{a}_{\text{out}}^9 j_\star^{37} c^{18} (m_2 + \mu/3)^{11}} \right]^{1/8}. \quad (51)$$

We can also calculate $\dot{I}_e/\bar{\Omega}_e$ from numerical simulations. Taking characteristic $\bar{I} \approx 120^\circ$ (Figs. 6 and 7 show that this holds across a range of I_0), we fit the last remaining free parameter f [Eq. (49)] to the data from numerical simulations. This

yields $f \approx 2.72$, leading to

$$\begin{aligned} \left| \frac{\dot{I}_e}{\bar{\Omega}_e} \right|_{\text{max}} &\simeq 0.98^\circ \left(\frac{\cos I_0}{\cos(90.3^\circ)} \right)^{-37/8} \left(\frac{\bar{a}_{\text{out}}}{2.2 \text{ pc}} \right)^{-9/8} \\ &\times \left(\frac{m_3}{3 \times 10^7 M_\odot} \right)^{3/8} \left(\frac{m_{12}^9 \mu^8 / (m_2 + \mu/3)^{11}}{(28.64 M_\odot)^6} \right)^{1/8}. \end{aligned} \quad (52)$$

Fig. 8 shows that when the merger time T_m is much larger than the initial LK timescale, Eq. (52) provides an accurate estimate for $|\dot{I}_e/\bar{\Omega}_e|_{\text{max}}$ when compared with numerical results.

In the above, we have assumed that the system evolves through $\mathcal{A} \simeq 1$ when the eccentricity is mostly frozen (see Fig. 1 for an indication of how accurate this is for the parameter space explored in Fig. 8). It is also possible that $\mathcal{A} \simeq 1$ occurs when the eccentricity is still undergoing substantial oscillations. In fact, Eq. (52) remains accurate in this case when replacing e with e_{max} , due to the following analysis. Recall that when $e_{\text{min}} \ll e_{\text{max}}$, the binary spends a fraction $\sim j(e_{\text{max}})$ of the LK cycle near $e \simeq e_{\text{max}}$. This fraction of the LK cycle dominates both GW dissipation and $\bar{\Omega}_e$ precession. Thus, both \dot{I}_e and $\bar{\Omega}_e$ in the oscillating- e regime can be evaluated by setting $e \approx e_{\text{max}}$ and multiplying by a prefactor

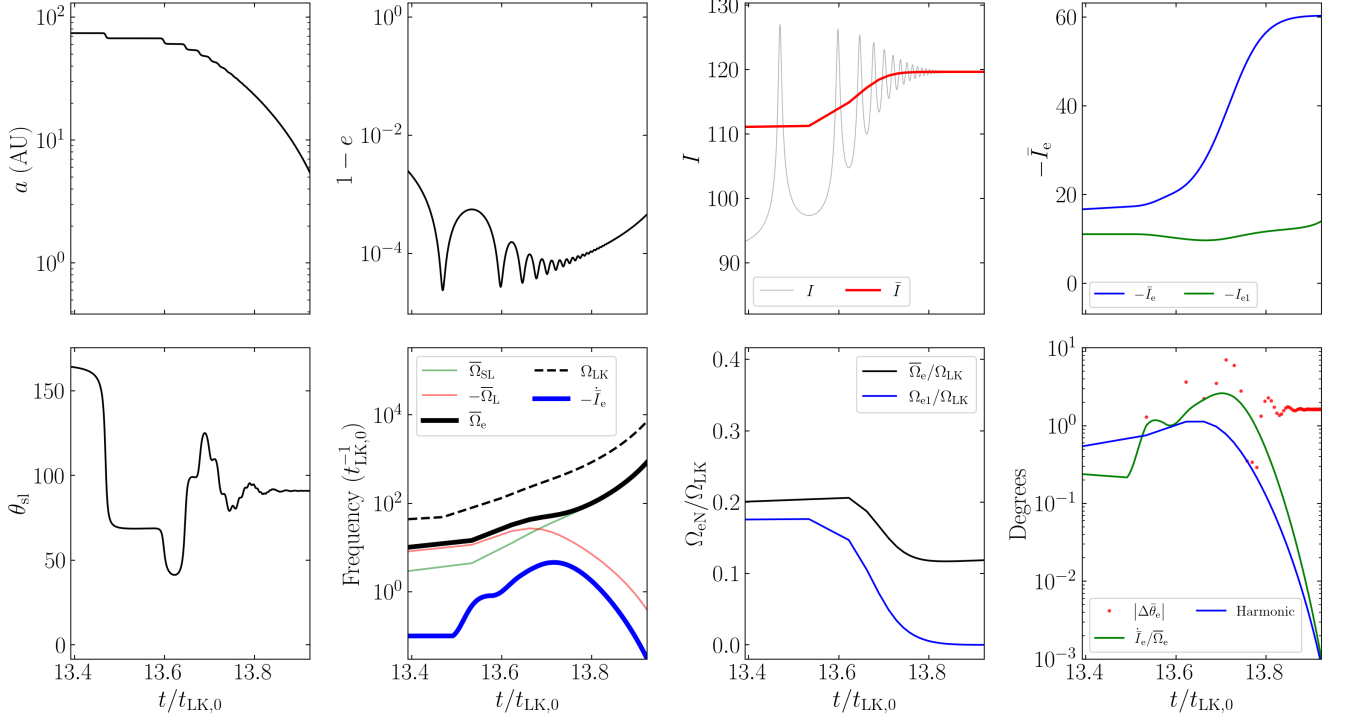


Figure 7. Same as Fig. 6 except for $I_0 = 90.2^\circ$ (and all other parameters are the same as in Fig. 1), corresponding to a faster coalescence. The total change in $\bar{\theta}_e$ for this simulation is $\approx 2^\circ$.

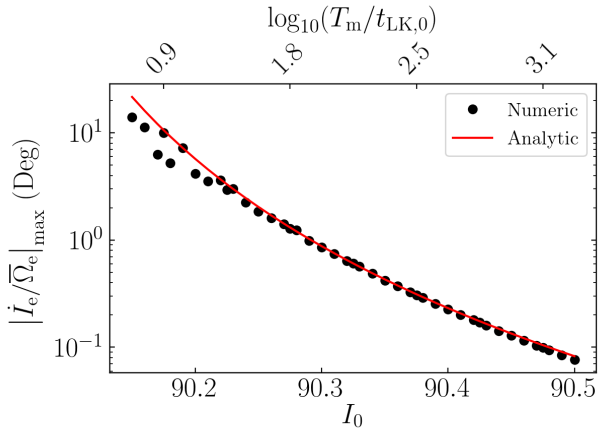


Figure 8. Comparison of $|I_e/\bar{\Omega}_e|_{\max}$ obtained from simulations and from the analytical expression Eq. (52), where we take $f = 2.72$ in Eq. (49). The coalescence time T_m is shown along the top axis of the plot in units of the characteristic LK timescale at the start of inspiral $t_{LK,0}$. The agreement between the analytical and numerical results is excellent for $T_m \gg t_{LK,0}$.

of $j(e_{\max})$. This factor cancels when computing the quotient $\dot{I}_e/\bar{\Omega}_e$.

The accuracy of Eq. (52) in bounding $|\Delta\bar{\theta}_e|^f$ is shown in Fig. 9, where we carry out simulations for a range of I_0 , and for each I_0 we consider 100 different, isotropically distributed

initial orientations for \mathbf{S} (thus sampling a wide range of initial $\bar{\theta}_e$). Note that conservation of $\bar{\theta}_e$ is generally much better than Eq. (52) predicts. This is because cancellation of phases in Eq. (40) is generally more efficient than Eq. (52) assumes (recall that Eq. (41) only provides an estimate for the amplitude of “local” oscillations of $\bar{\theta}_e$). Nevertheless, it is clear that Eq. (52) provides a robust upper bound of $|\Delta\bar{\theta}_e|^f$, and serves as a good indicator for the breakdown of adiabatic invariance.

4.4. Origin of the $\theta_{sl}^f = 90^\circ$ Attractor

In Fig. 2, we show θ_{sl}^f as a function of I_0 when $\theta_{sl}^i = 0$. With the results developed in the previous sections, we can understand the behavior seen in this plot.

First, while $\bar{\theta}_e$ is our proposed adiabatic invariant, $\bar{\theta}_e^i$ is not measurable. As such, we re-express $\bar{\theta}_e$ in terms of physical quantities. We work in the inertial frame and choose spherical coordinate system where $\mathbf{L}_{out} \propto \hat{\mathbf{Z}}$. We then specify \mathbf{S} by the polar and azimuthal angles θ_{s3} and ϕ_{s3} respectively. We follow the same convention as before and choose $\hat{\mathbf{X}}$ to point along $\hat{\mathbf{L}}$. Finally, we will consider the case of nonzero $\eta \equiv L/L_{out}$ here, to better parallel the discussion in LL18. In this case, $\bar{\Omega}_e$ is given by (Liu & Lai 2017)

$$\bar{\Omega}_e = \bar{\Omega}_{SL}\hat{\mathbf{L}} + \bar{\Omega}_L \frac{\mathbf{L}_{tot}}{L_{out}}, \quad (53)$$

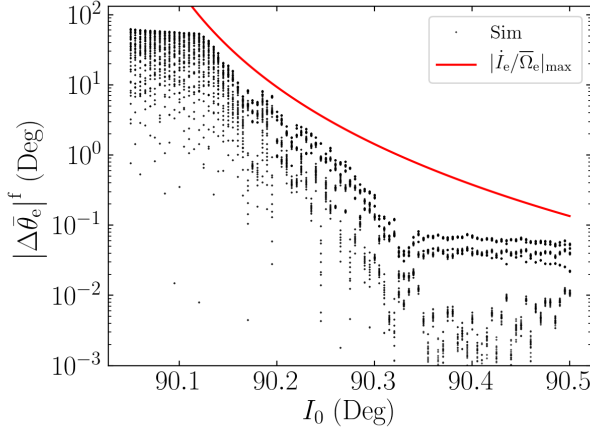


Figure 9. Net change in $\bar{\theta}_e$ over the binary inspiral as a function of initial inclination I_0 . For each I_0 , 100 simulations are run for \mathbf{S} on a uniform, isotropic grid. Plotted for comparison is the bound $|\Delta\bar{\theta}_e|^f \lesssim |\dot{\bar{I}}_e/\bar{\Omega}_e|_{\max}$, using the analytical expression given by Eq. (52). It is clear that the expression provides a robust upper bound for the non-conservation of $\bar{\theta}_e$ due to nonadiabatic effects. Note that at the right of the plot, the numerical $|\Delta\bar{\theta}_e|^f$ saturates; this is because we compute the initial $\bar{\Omega}_e$ (in order to evaluate the initial $\bar{\theta}_e$) without GW dissipation, and such a procedure inevitably introduces fuzziness in $\bar{\theta}_e$.

where

$$\mathbf{L}_{\text{tot}} \equiv \mathbf{L} + \mathbf{L}_{\text{out}}. \quad (54)$$

It can then be shown that

$$\bar{\Omega}_e = \bar{\Omega}_L [(\mathcal{A} + \eta) \sin \bar{I} \hat{\mathbf{X}} + (\mathcal{A} \cos \bar{I} + \eta \cos \bar{I} + 1) \hat{\mathbf{Z}}]. \quad (55)$$

Then, for some $\mathbf{S} = \cos \theta_{s3} \hat{\mathbf{Z}} + \sin \theta_{s3} (\cos \phi_{s3} \hat{\mathbf{X}} + \sin \phi_{s3} \hat{\mathbf{Y}})$, we can evaluate and find

$$\cos \bar{\theta}_e = \frac{(\mathcal{A} + \eta) \cos \theta_{sl} \pm \cos \theta_{s3}}{\sqrt{(\mathcal{A} + \eta)^2 \pm 2(\mathcal{A} + \eta) \cos \bar{I} + 1}}. \quad (56)$$

The sign in the above equation is equal to $\text{sgn}(\bar{\Omega}_L)$, i.e. positive for $I_0 < 90^\circ$ and negative for $I_0 > 90^\circ$. Our equation is in agreement with Eq. (73) of LL18 when taking $\theta_{sl} = 0$ [since they evaluate for $e_0 \approx 0$, their $\mathcal{A}_0/2 \cos I_0$ is our \mathcal{A} ; see their Eq. (72)].

Note that, for the fiducial parameter space, $\mathcal{A} \ll 1$ initially (Fig. 5), and $\eta \ll 1$ as well, so Eq. (56) simply gives

$$\bar{\theta}_e^i \approx \begin{cases} \theta_{sb}^i & I_0 < 90^\circ, \\ 180^\circ - \theta_{sb}^i & I_0 > 90^\circ, \end{cases} \quad (57)$$

On the other hand, at late times, $\mathcal{A} \gg 1$, and $\bar{\theta}_e^f = \theta_{sl}^f$. Thus, when $\bar{\theta}_e$ is conserved, we obtain

$$\theta_{sl}^f \approx \begin{cases} \theta_{sb}^i & I_0 < 90^\circ, \\ 180^\circ - \theta_{sb}^i & I_0 > 90^\circ, \end{cases} \quad (58)$$

This shows that we expect $\theta_{sl}^f \in [89.5^\circ, 90^\circ]$ for mergers in Fig. 2 sufficiently far from $I_0 = 90^\circ$, which is indeed observed. This is the origin of the 90° attractor. This is further in agreement with the recent results in Yu et al. (2020), where they studied arbitrary initial \mathbf{S}_i orientations and obtained exactly Eq. (58) [see their Eq. (46), bottom panel of Fig. 4].

So far, we have analyzed the θ_{sl}^f distribution for smooth mergers. Next, we can consider rapid mergers, for which $\bar{\theta}_e$ conservation is imperfect. We expect

$$|\theta_{sl}^f - \bar{\theta}_e^i| \lesssim |\Delta\bar{\theta}_e|^f. \quad (59)$$

where $|\Delta\bar{\theta}_e|^f$ is given by Eq. (52). This is overplotted as the black dotted line in Fig. 2, and we see it mostly captures the deviation of θ_{sl}^f from $\sim 90^\circ$ except very near $I_0 = 90^\circ$. This is expected, as Eq. (52) is singular for $I_0 = 90^\circ$, and it is expected to lose accuracy in this regime as shown in Fig. 9.

When $I_0 = 90^\circ$ exactly, we can show that $\theta_{sl}^f = \theta_{sl}^i$: when $I_0 = 90^\circ$, $dI/dt = 0$ by Eq. (7), so $I = 90^\circ$ for all time. Then, $d\bar{\Omega}/dt = 0$ for $I = 90^\circ$ [Eq. (6)], implying that \mathbf{L} is constant. Thus, \mathbf{S} precesses around fixed \mathbf{L} , and θ_{sl} can never change. For Fig. 2, we take $\theta_{sl}^i = 0$, and indeed we see that $\theta_{sl}^f = 0$ at $I_0 = 90^\circ$ in the figure.

Finally, Fig. 2 shows that the true θ_{sl}^f are oscillatory within the envelope bounded by Eq. (59) above. This can also be understood: Eq. (42) only bounds the maximum of the absolute value of the change in $\bar{\theta}_e$, while the actual change depends on the initial and final complex phases of S_\perp in Eq. (40), denoted $\Phi(t_i)$ and $\Phi(t_f)$. When $\theta_{sl}^i = 0$, we have $\Phi(t_i) = 0$, as \mathbf{S} starts in the $\hat{\mathbf{x}}\text{-}\hat{\mathbf{z}}$ plane. Then, as I_0 is smoothly varied, the final phase $\Phi(t_f)$ must also vary smoothly [since $\bar{\Omega}_e$ in Eq. (39) is a continuous function, $\Phi(t)$ must be as well], so the total phase difference between the initial and final values of S_\perp varies smoothly. This means the total change in $\bar{\theta}_e$ will fluctuate smoothly between $\pm |\Delta\bar{\theta}_e|^f$ as I_0 is changed, giving rise to the sinusoidal shape seen in Fig. 2.

5. ANALYSIS: EFFECT OF RESONANCES

In the previous section, we neglected the $N \geq 1$ Fourier harmonics in Eq. (25), and showed that the final θ_{sl}^f behavior could be completely explained. In this section, we study one effect of the Fourier harmonics that occurs when two frequencies become commensurate. We show this effect can be neglected for the fiducial parameter regime. A regime for which the Fourier harmonics cannot be neglected is discussed separately in Section 6.

For simplicity, we ignore the effects of GW dissipation in this section and assume the system is exactly periodic (so $\dot{I}_e = 0$). The scalar equation of motion Eq. (34) is then:

$$\frac{dS_\perp}{dt} = i\bar{\Omega}_e S_\perp + \sum_{N=1}^{\infty} [\cos(\Delta I_{eN}) S_\perp - i \cos \theta \sin(\Delta I_{eN}) \Omega_{eN} \cos(N\Omega_{LK}t)]. \quad (60)$$

Resonances can occur when $\bar{\Omega}_e = N\Omega_{LK}$. Numerically, we find that $\bar{\Omega}_e \lesssim \Omega_{LK}$ for most regions of parameter space (see Fig. 10, and recall that LK-induced mergers only complete within a Hubble time when $I_{\min} \approx 90^\circ$). Accordingly, we restrict our analysis to resonances with the $N = 1$ component. For simplicity, we also ignore the modulation of the forcing frequency in Eq. (60). While this fails to capture the possibility of a parametric resonance, we find no evidence for parametric resonances in our simulations. With these two simplifications, Eq. (60) further reduces to

$$\frac{dS_\perp}{dt} \approx i\bar{\Omega}_e S_\perp - i \cos \bar{\theta}_e \sin(\Delta I_{e1}) \Omega_{e1} \cos(\Omega_{LK} t). \quad (61)$$

We can approximate $\cos(\Omega_{LK} t) \approx e^{i\Omega_{LK} t}/2$, as the $e^{-i\Omega_{LK} t}$ component is far from resonance. Then we can write down solution as before

$$e^{-i\bar{\Omega}_e t} S_\perp \Big|_{t_i}^{t_f} = - \int_{t_i}^{t_f} \frac{i \sin(\Delta I_{e1}) \Omega_{e1}}{2} e^{-i\bar{\Omega}_e t + i\Omega_{LK} t} \cos \bar{\theta}_e dt. \quad (62)$$

Thus, similarly to Section 4.2, the instantaneous oscillation amplitude $|\Delta \bar{\theta}_e|$ can be bound by

$$|\Delta \bar{\theta}_e| \sim \frac{1}{2} \left| \frac{\sin(\Delta I_{e1}) \Omega_{e1}}{\Omega_{LK} - \bar{\Omega}_e} \right|. \quad (63)$$

We see that if $\bar{\Omega}_e < \Omega_{LK}$ by a sufficient margin for all times, then the conservation of $\bar{\theta}_e$ in the fiducial parameter regime cannot be significantly affected by this resonance. The ratio $\bar{\Omega}_e/\Omega_{LK}$ is shown in the middle panel of Fig. 5, and the amplitude of oscillation of $\bar{\theta}_e$ it generates [Eq. (63)] is given in blue in the bottom panel of Fig. 5. We see that the total effect of the harmonic terms never exceeds a few degrees.

Furthermore, we see from Fig. 6 (top rightmost panel and third panel of bottom row) that the interesting dynamics, occurring when Ω_{e1} and ΔI_{e1} are both nonzero [necessary for Eq. (63) to be nonzero], occur in the regime $\mathcal{A} \approx 1$. Then, the bottom-rightmost panel of Fig. 6 compares the detailed behavior of $\bar{\theta}_e$ and its two contributions, the nonadiabatic and harmonic effects. We see that Eq. (63) describes the oscillations in $\bar{\theta}_e$ very well. The agreement is poorer in the bottom-rightmost panel of Fig. 7, as the nonadiabatic effect is much stronger. However, note that the theory presented in the previous section captures the final deviations $|\Delta \bar{\theta}_e|^f$ very well (see Fig. 9 for $I_0 = 90.35^\circ$). This suggests that oscillations in $\bar{\theta}_e$ due to harmonic perturbations of up to a few degrees do not affect final nonconservation by more than $\sim 0.01^\circ$.

6. LIDOV-KOZAI ENHANCED MERGERS

In LL17, a different parameter regime is considered, where the inner binary is sufficiently close in (~ 0.1 AU) that it can

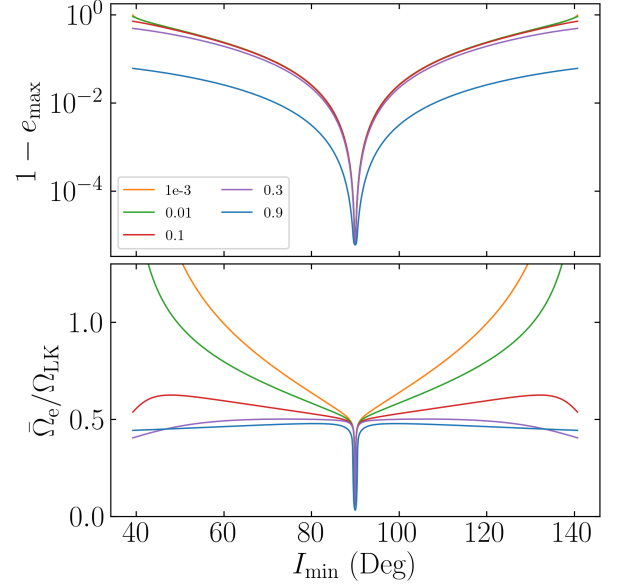


Figure 10. e_{\max} and $\bar{\Omega}_e/\Omega_{LK}$ as a function of I_{\min} , the inclination of the inner binary at eccentricity minimum, for varying values of e_{\min} (different colors) for the fiducial parameter regime.

merge in isolation via GW radiation, given by: $m_1 = m_2 = m_3 = 30M_\odot$, $a_{\text{in}} = 0.1$ AU, $\tilde{a}_{\text{out}} = 3$ AU, and $e_{\text{out}} = 0$. Note that m_3 here is not an SMBH. However, our results can still be applied judiciously to this parameter regime and yield interesting insights.

First, we recall the θ_{sl}^f distribution obtained via numerical simulation, shown in Fig. 11. LL17 derives an adiabatic invariant assuming the inner binary does not undergo eccentricity oscillations. Our result, based on $\bar{\theta}_e$ conservation, is a generalization of their result, giving the same result when the inner orbit remains circular. Very near $I_0 \approx 90^\circ$, the data are offset somewhat from our result, because we have assumed the tertiary's angular momentum is fixed, but accounting for the offset, our theory captures the scaling of θ_{sl}^f , as seen in Fig. 12.

However, as can be seen in Fig. 11, intermediate inclinations $I_0 \in [50, 80]$ and $I_0 \in [100, 130]$ exhibit very volatile behavior in θ_{sl}^f . This is unlike the plots generated in the fiducial parameter regime (Fig. 2), as this inclination regime corresponds to neither the fastest nor slowest merging systems. We attribute the origin of this volatility to a stronger resonant interaction. By examining Fig. 13, it is evident that, for the same e_{\min} , systems with I_{\min} further from 90° are closer to the $\bar{\Omega}_e = \Omega_{LK}$ resonance. Outside of the LK window, $\bar{\Omega}_e$ also goes swiftly to zero, as seen in Fig. 13, so this explanation is consistent with the ranges of inclinations that exhibit volatile θ_{sl}^f behavior. We forgo further investigation of this mechanism because it is not expected to play an impor-

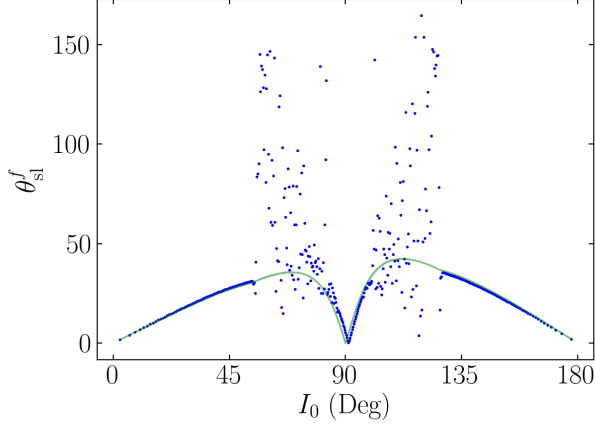


Figure 11. Plot of θ_{sl}^f for the LK-enhanced parameter regime, i.e. $m_1 = m_2 = m_3 = 30M_\odot$, $a_{in} = 0.1$ AU, $a_{out} = 3$ AU, and $e_{out} = 0$. Conservation of $\bar{\theta}_e$ gives the green line. Agreement near $I_0 = 90^\circ$ is good when accounting for the effects of a finite L_{out} (see Fig. 12). For I_0 in the two intervals $[40^\circ, 80^\circ]$ and $[100^\circ, 140^\circ]$, a further effect causes θ_{sl}^f to fluctuate unpredictably.

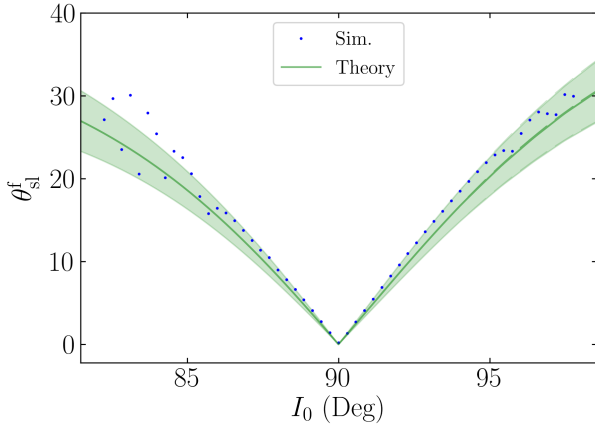


Figure 12. Zoomed in version of Fig. 11 near $I_0 \approx 90^\circ$ while adding an I_0 offset to account for differences between the data and theory due to finite L_{out} effects. The green shaded area shows the expected range of deviations due to resonant perturbations following Eq. (63) (evaluated for the initial system parameters). The data nearer 90° have less spread than predicted, but the transition to a larger θ_{sl}^f spread roughly follows the prediction of the green line.

tant role in any LK-induced BH binary mergers for reasons discussed below.

At first, it seems clear from Fig. 10 that $\bar{\Omega}_e$ is significantly smaller than Ω_{LK} near $I_{min} \approx 90^\circ$ for LK-induced mergers. However, this is not sufficient to guarantee that the frequency ratio remains small for the entire evolution, as GR effects become stronger as the binary coalesces. Instead, a more

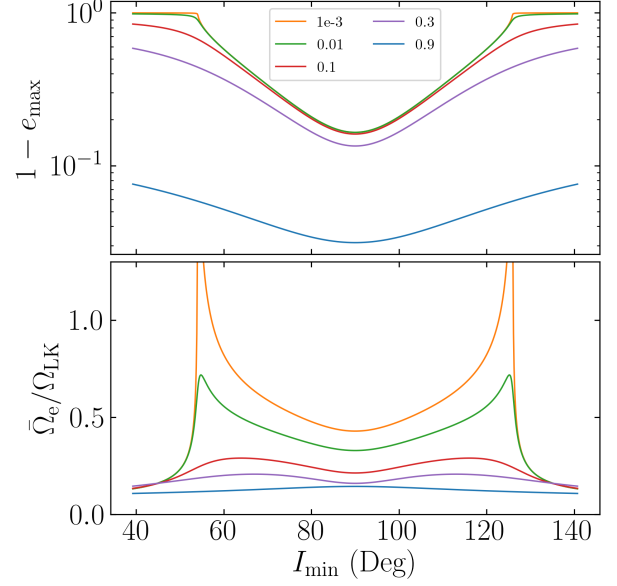


Figure 13. Same as Fig. 10 but for the compact parameter regime. Compared to Fig. 10, we see that e_{max} is smaller due to stronger pericenter precession Ω_{GR} in this regime, so the $\bar{\Omega}_e / \Omega_{LK} = 1$ resonance is accessible for a wide range of parameter space. In particular, both smaller e_{min} and e_{max} values bring the system closer to the resonance.

careful analysis of the relevant quantities in Eq. (63) proves useful:

- $\sin(\Delta I_{e1})$ is small unless $\mathcal{A} \approx 1$. Otherwise, Ω_e does not nutate appreciably within an LK cycle, and all the Ω_{eN} are aligned with Ω_e , implying all the $\Delta I_{eN} \approx 0$.
- Smaller values of e_{min} increase $\bar{\Omega}_e / \Omega_{LK}$, as shown in Fig. 13.

However, LK-driven coalescence causes \mathcal{A} to increase on a similar timescale to that of e_{min} increase (see Fig. 1). This implies that, if $\mathcal{A} \ll 1$ initially, which is the case for LK-induced mergers, then e_{min} will be very close to 1 when \mathcal{A} grows to be ≈ 1 , and the contribution predicted by Eq. (63) must be small.

7. CONCLUSION AND DISCUSSION

In this paper, we consider the evolution of the spin-orbit misalignment angle θ_{sl} of a black hole (BH) binary that merges under gravitational wave (GW) radiation during Lidov-Kozai (LK) oscillations induced by a tertiary supermassive black hole (SMBH). We show that, when the gravitational potential of the SMBH is handled at quadrupolar order, the spin vectors of the inner BHs obey the simple equation of motion Eq. (22). Analysis of this equation yields the following conclusions:

- Since Eq. (22) is a linear system with periodically varying coefficients, it cannot give rise to chaotic dynamics by Floquet’s Theorem.
- For most parameters of astrophysical relevance, the angle $\bar{\theta}_e$ [Eq. (36)] is an adiabatic invariant. Since the inner BH binary merges in finite time, $\bar{\theta}_e$ is only conserved to finite accuracy; we show that the deviation from perfect adiabaticity can be predicted from initial conditions.
- When the resonant condition $\bar{\Omega}_e \approx \Omega_{LK}$ is satisfied, significant oscillations in $\bar{\theta}_e$ can arise. We derive an analytic estimate of this oscillation amplitude. This estimate both demonstrates that the resonance is unimportant for “LK-induced” mergers and tentatively explains the scatter in θ_{sl}^f seen by LL17.

REFERENCES

- Abbott, B., et al. 2016, *Phys. Rev. Lett.*, 116, 061102, doi: [10.1103/PhysRevLett.116.061102](https://doi.org/10.1103/PhysRevLett.116.061102)
- Abbott, B., Abbott, R., Abbott, T., et al. 2019, *The Astrophysical Journal Letters*, 882, L24
- Anderson, K. R., Storch, N. I., & Lai, D. 2016, *Monthly Notices of the Royal Astronomical Society*, 456, 3671
- Antonini, F., & Perets, H. B. 2012, *The Astrophysical Journal*, 757, 27
- Antonini, F., Rodriguez, C. L., Petrovich, C., & Fischer, C. L. 2018, *Monthly Notices of the Royal Astronomical Society: Letters*, 480, L58
- Antonini, F., Toonen, S., & Hamers, A. S. 2017, *The Astrophysical Journal*, 841, 77
- Banerjee, S., Baumgardt, H., & Kroupa, P. 2010, *Monthly Notices of the Royal Astronomical Society*, 402, 371
- Belczynski, K., Dominik, M., Bulik, T., et al. 2010, *The Astrophysical Journal Letters*, 715, L138
- Belczynski, K., Holz, D. E., Bulik, T., & O’Shaughnessy, R. 2016, *Nature*, 534, 512
- Belczynski, K., Klencki, J., Fields, C., et al. 2020, *Astronomy & Astrophysics*, 636, A104
- Blaes, O., Lee, M. H., & Socrates, A. 2002, *The Astrophysical Journal*, 578, 775
- Dominik, M., Belczynski, K., Fryer, C., et al. 2012, *The Astrophysical Journal*, 759, 52
- . 2013, *The Astrophysical Journal*, 779, 72
- Dominik, M., Berti, E., O’Shaughnessy, R., et al. 2015, *The Astrophysical Journal*, 806, 263
- Downing, J., Benacquista, M., Giersz, M., & Spurzem, R. 2010, *Monthly Notices of the Royal Astronomical Society*, 407, 1946
- Floquet, G. 1883, in *Annales scientifiques de l’École normale supérieure*, Vol. 12, 47–88
- Gondán, L., Kocsis, B., Raffai, P., & Frei, Z. 2018, *The Astrophysical Journal*, 860, 5
- Hoang, B.-M., Naoz, S., Kocsis, B., Rasio, F. A., & Dosopoulou, F. 2018, *The Astrophysical Journal*, 856, 140
- Kinoshita, H. 1993, *Celestial Mechanics and Dynamical Astronomy*, 57, 359
- Kuchment, P. A. 2012, *Floquet theory for partial differential equations*, Vol. 60 (Birkhäuser)
- Lipunov, V., Postnov, K., & Prokhorov, M. 1997, *Astronomy Letters*, 23, 492
- Lipunov, V., Kornilov, V., Gorbovskoy, E., et al. 2017, *Monthly Notices of the Royal Astronomical Society*, 465, 3656
- Liu, B., & Lai, D. 2017, *The Astrophysical Journal Letters*, 846, L11
- . 2018, *The Astrophysical Journal*, 863, 68
- Liu, B., Lai, D., & Wang, Y.-H. 2019, *The Astrophysical Journal*, 881, 41
- Miller, M. C., & Hamilton, D. P. 2002, *The Astrophysical Journal*, 576, 894
- Miller, M. C., & Lauburg, V. M. 2009, *The Astrophysical Journal*, 692, 917
- O’leary, R. M., Rasio, F. A., Fregeau, J. M., Ivanova, N., & O’Shaughnessy, R. 2006, *The Astrophysical Journal*, 637, 937
- Podsiadlowski, P., Rappaport, S., & Han, Z. 2003, *Monthly Notices of the Royal Astronomical Society*, 341, 385
- Postnov, K., & Kuranov, A. 2019, *Monthly Notices of the Royal Astronomical Society*, 483, 3288
- Randall, L., & Xianyu, Z.-Z. 2018, *The Astrophysical Journal*, 853, 93
- Rodriguez, C. L., Amaro-Seoane, P., Chatterjee, S., & Rasio, F. A. 2018, *Physical Review Letters*, 120, 151101
- Rodriguez, C. L., Morscher, M., Pattabiraman, B., et al. 2015, *Physical Review Letters*, 115, 051101
- Samsing, J., & D’Orazio, D. J. 2018, *Monthly Notices of the Royal Astronomical Society*, 481, 5445
- Samsing, J., & Ramirez-Ruiz, E. 2017, *The Astrophysical Journal Letters*, 840, L14
- Schmidt, P., Ohme, F., & Hannam, M. 2015, *Physical Review D*, 91, 024043
- Silsbee, K., & Tremaine, S. 2016, arXiv preprint arXiv:1608.07642
- Storch, N. I., Anderson, K. R., & Lai, D. 2014, *Science*, 345, 1317
- Storch, N. I., & Lai, D. 2015, *Monthly Notices of the Royal Astronomical Society*, 448, 1821

- Storch, N. I., Lai, D., & Anderson, K. R. 2017, *Monthly Notices of the Royal Astronomical Society*, 465, 3927
- Wen, L. 2003, *The Astrophysical Journal*, 598, 419
- Yu, H., Ma, S., Giesler, M., & Chen, Y. 2020, arXiv preprint arXiv:2007.12978
- Ziosi, B. M., Mapelli, M., Branchesi, M., & Tormen, G. 2014, *Monthly Notices of the Royal Astronomical Society*, 441, 3703
- Zwart, S. F. P., & McMillan, S. L. 1999, *The Astrophysical Journal Letters*, 528, L17